spectrum of the laser using a scanning Fabry–Pérot spectrum analyser. We see that the laser has multiple cavity modes with a mode spacing of ~0.9 GHz, which corresponds to the free spectral range of a 4.8-cm-long silicon waveguide cavity.

This demonstration of Raman lasing in a silicon waveguide cavity on a single chip represents a significant step towards a more practical, all-silicon-based, c.w. amplifier or laser. We note that the multi-layer coatings are not essential for this device, and that single chip resonators may be fabricated using waveguide Bragg reflectors or ring resonator architectures; both these alternatives are compatible with CMOS processing. Further reduction in the carrier lifetime or cavity optimization could lead to c.w. Raman lasing in silicon. □

Received 23 October; accepted 10 December 2004; doi:10.1038/nature03273.
Published online 5 January 2005.

1. Pavesi, L., Gaponenko, S. & Dal Negro, L. (eds) *Towards the First Silicon Laser* (NATO science series, Kluwer, Dordrecht, 2003).
2. Shimizu-Iwayama, T. *et al.* Visible photoluminescence in Si^+-implanted silica glass. *J. Appl. Phys.* **75,** 7779–7783 (1994).
3. Brongersma, M. L., Polman, A., Min, K. S., Tambo, T. & Atwater, H. A. Tuning the emission wavelength of Si nanocrystals in SiO_2 by oxidation. *Appl. Phys.* **72,** 2577–2579 (1998).
4. Iacona, F., Franzo, G. & Spinella, C. Correlation between luminescence and structural properties of Si nanocrystals. *J. Appl. Phys.* **87,** 1295–1303 (2000).
5. Pavesi, L., Negro, L. D., Mazzoleni, C., Franzo, G. & Priolo, F. Optical gain in silicon nanocrystals. *Nature* **408,** 440–444 (2000).
6. Lockwood, D. J., Lu, Z. H. & Baribeau, J. M. Quantum confined luminescence in Si/SiO_2 superlattices. *Phys. Rev. Lett.* **76,** 539–541 (1996).
7. Lombardo, S., Campisano, S. U., van den Hoven, G. N., Cacciato, A. & Polman, A. Room-temperature luminescence from Er^{3+}-implanted semi-insulating polycrystalline silicon. *Appl. Phys. Lett.* **63,** 1942–1944 (1993).
8. Fujii, M., Yoshida, M., Kanzawa, Y., Hayashi, S. & Yamamoto, K. 1.54 μm photoluminescence of Er^{3+} doped into SiO_2 films containing Si nanocrystals: evidence for energy transfer from Si nanocrystals to Er^{3+}. *Appl. Phys. Lett.* **71,** 1198–1200 (1997).
9. Kik, P. G., Brongersma, M. L. & Polman, A. Strong exciton-erbium coupling in Si nanocrystal-doped SiO_2. *Appl. Phys. Lett.* **76,** 2325–2327 (2000).
10. Han, H. S., Seo, S. Y. & Shin, J. H. Optical gain at 1.54 μm in erbium-doped nanocluster sensitized waveguide. *Appl. Phys. Lett.* **79,** 4568–4570 (2001).
11. Trupke, T., Zhao, J., Wang, A., Corkish, R. & Green, M. Very efficient light emission from bulk crystalline silicon. *Appl. Phys. Lett.* **82,** 2996–2998 (2003).
12. Dehlinger, G. *et al.* Intersubband electroluminescence from silicon-based quantum cascade structures. *Science* **290,** 2277–2280 (2000).
13. Claps, R., Dimitropoulos, D., Han, Y. & Jalali, B. Observation of Raman emission in silicon waveguides at 1.54 μm. *Opt. Express* **10,** 1305–1313 (2002).
14. Claps, R., Dimitropoulos, D., Raghunathan, V., Han, Y. & Jalali, B. Observation of stimulated Raman amplification in silicon waveguides. *Opt. Express* **11,** 1731–1739 (2003).
15. Liang, T. K. & Tsang, H. K. Role of free carriers from two-photon absorption in Raman amplification in silicon-on-insulator waveguides. *Appl. Phys. Lett.* **84,** 2745–2747 (2004).
16. Espinola, R. L., Dadap, J. I., Osgood, R. M. Jr, McNab, S. J. & Vlasov, Y. A. Raman amplification in ultrasmall silicon-on-insulator wire waveguides. *Opt. Express* **12,** 3713–3718 (2004).
17. Rong, H. *et al.* Raman gain and nonlinear optical absorption measurement in a low loss silicon waveguide. *Appl. Phys. Lett.* **85,** 2196–2198 (2004).
18. Liu, A., Rong, H., Paniccia, M., Cohen, O. & Hak, D. Net optical gain in a low loss silicon-on-insulator waveguide by stimulated Raman scattering. *Opt. Express* **12,** 4261–4267 (2004).
19. Xu, Q., Almeida, V. & Lipson, M. Time-resolved study of Raman gain in highly confined silicon-on-insulator waveguides. *Opt. Express* **12,** 4437–4442 (2004).
20. Liang, T. K. & Tsang, H. K. Efficient Raman amplification in silicon-on-insulator waveguides. *Appl. Phys. Lett.* **85,** 3343–3345 (2004).
21. Boyraz, O. & Jalali, B. Demonstration of 11dB fiber-to-fiber gain in a silicon Raman amplifier. *IEICE Elect. Express* **1,** 429–434 (2004).
22. Boyraz, O. & Jalali, B. Demonstration of a silicon Raman laser. *Opt. Express* **12,** 5269–5273 (2004).
23. Agrawal, G. P. *Nonlinear Fiber Optics* 2nd edn (Academic, New York, 1995).
24. Reed, G. T. & Knights, A. P. *Silicon Photonics: An Introduction* (John Wiley, Chichester, UK, 2004).
25. Tsang, H. K. *et al.* Optical dispersion, two photon absorption and self-phase modulation in silicon waveguides at 1.5 μm wavelength. *Appl. Phys. Lett.* **80,** 416–418 (2002).
26. Dinu, M., Quochi, F. & Garcia, H. Third-order nonlinearities in silicon telecom wavelengths. *Appl. Phys. Lett.* **82,** 2954–2956 (2003).
27. Soref, R. A. & Lorenzo, P. J. All-silicon active and passive guided-wave components for λ = 1.3 and 1.6 μm. *IEEE J. Quant. Electron.* **QE-22,** 873–879 (1986).

Acknowledgements We thank A. Alduino, D. Tran, J. Tseng, D. Hodge and J. Johnson for assistance in device fabrication and sample preparation; S. Koehl for software development; M. Morse, H. Liu, M. Salib, D. Samararubio, L. Liao, R. Li and G. Ding for technical discussions; and G. T. Reed, I. P. Kaminow and J. E. Bowers for conversations.

Competing interests statement The authors declare that they have no competing financial interests.

Correspondence and requests for materials should be addressed to H.R. (haisheng.rong@intel.com).

Stable sea surface temperatures in the western Pacific warm pool over the past 1.75 million years

Thibault de Garidel-Thoron[1], Yair Rosenthal[1,2], Franck Bassinot[3] & Luc Beaufort[4]

[1]*Institute of Marine and Coastal Sciences-Rutgers University, 71 Dudley Road, and*
[2]*Department of Geological Sciences-Rutgers University, New Brunswick, New Jersey 08901, USA*
[3]*Laboratoire des Sciences du Climat et de l'Environnement–CEA, 91198 Gif-sur-Yvette cedex, France*
[4]*CEREGE-CNRS Université Aix-Marseille 3, BP80, 135345 Aix-en-Provence cedex 4, France*

About 850,000 years ago, the period of the glacial cycles changed from 41,000 to 100,000 years. This mid-Pleistocene climate transition has been attributed to global cooling, possibly caused by a decrease in atmospheric carbon dioxide concentrations[1,2]. However, evidence for such cooling is currently restricted to the cool upwelling regions in the eastern equatorial oceans[3,4], although the tropical warm pools on the western side of the ocean basins are particularly sensitive to changes in radiative forcing[5,6]. Here we present high-resolution records of sea surface temperatures spanning the past 1.75 million years, obtained from oxygen isotopes and Mg/Ca ratios in planktonic foraminifera from the western Pacific warm pool. In contrast with the eastern equatorial regions, sea surface temperatures in the western Pacific warm pool are relatively stable throughout the Pleistocene epoch, implying little long-term change in the tropical net radiation budget. Our results challenge the hypothesis of a gradual decrease in atmospheric carbon dioxide concentrations as a dominant trigger of the longer glacial cycles since 850,000 years ago. Instead, we infer that the temperature contrast across the equatorial Pacific Ocean increased, which might have had a significant influence on the mid-Pleistocene climate transition.

The warmest pool of oceanic surface lies in the western equatorial Pacific Ocean and plays an important role in Earth's climate. Annual sea surface temperatures (SSTs) above 28 °C (ref. 7) lead to deep atmospheric convection, which transfers through the atmosphere large amounts of water vapour and latent heat from tropical to mid-latitudes. The importance of the western equatorial Pacific warm pool (WPWP) is perhaps best manifested by the impact of the El Niño/Southern Oscillation (ENSO) on the interannual variability in the Earth's temperature and precipitation patterns[8,9]. ENSO-linked changes in tropical SST patterns also have a major influence on heat transport from low to mid- and high latitudes[10] and models suggest that long-term changes of SST patterns in the equatorial Pacific may also have had large consequences for extra-tropical climate in the past[11]. Thus, reconstructing past changes in tropical Pacific SSTs is critical for understanding the evolution of global heat and moisture transport, such as those occurring during the mid-Pleistocene transition, characterized by the onset of the large 100-kyr glacial cycles, about 0.85 Myr ago.

Here, we present a high-resolution Pleistocene record (0–1.75 Myr ago, Marine Isotopic Stages MIS1 to MIS59) of paired $\delta^{18}O$ and Mg/Ca measurements in planktonic foraminifera (*Globigerinoides ruber*, 250–300 μm, white) (Fig. 1) from the IMAGES core MD97-2140 located in the heart of the WPWP (2° 02′ N, 141° 46′ E, 2,547 m; Supplementary Fig. S1). The record extends the previously published, late-Pleistocene Ocean Drilling Program (ODP) site 806B record (0–450 kyr ago) from the Ontong-Java plateau[12], thus providing new insights on tropical Pacific climate variability during

the early Pleistocene. The records demonstrate that the mid-Pleistocene transition from 41-kyr- to 100-kyr-dominated periodicities, previously shown in high-latitude cores and more recently in the eastern equatorial Pacific[4], is also a prominent feature of the WPWP climate. Spectral analysis of the $\delta^{18}O$ and Mg/Ca records shows a dominant 41-kyr peak between 1,478 and 900 kyr ago and a 100-kyr peak between 850 and 6 kyr ago (Fig. 2). Thus, the WPWP record indicates that the early-Pleistocene obliquity-related oscillation observed in the eastern equatorial Pacific[4] was not limited to upwelling regions, but rather included the entire tropical Pacific. The onset of the 100-kyr cycle in the WPWP is accompanied by a significant increase in the amplitude of the glacial–interglacial $\delta^{18}O_{G.\ ruber}$. Between 1.75 and 0.85 Myr ago the glacial–interglacial amplitude (see Methods) in MD97-2140 is about 0.6 ± 0.2‰, whereas during the late Pleistocene the amplitude increased to about 1 ± 0.3‰, reaching 1.4‰ during terminations I, II and IV. Although the shift in the dominant frequency and glacial–interglacial amplitude at about 0.85 Myr ago is consistent with other Pleistocene records (see ref. 13 for example), the WPWP record is unique in that it shows no discernible long-term trend in $\delta^{18}O_{G.\ ruber}$, and remains at about −1.8‰ with a variance around this mean of ±0.6‰ throughout the Pleistocene.

The Mg/Ca-derived SST record also exhibits the change in periodicity 0.85 Myr ago (Fig. 1b) and, like $\delta^{18}O$, shows no long-term trend throughout the Pleistocene. As the core is situated above the modern lysocline, dissolution effects on our SST record are considered to be minimal. In support of this conclusion, our late-Holocene estimate of ~28.7 ± 0.5 °C is in close agreement with the modern mean annual SST of 28.6 °C in this region[7], and our estimated ~2.7 ± 0.5 °C cooling of the tropical Pacific during the last and penultimate glaciations accord with previous studies[12,14]. On a longer timescale, the late-Pleistocene part of our record is generally consistent with the ODP806B SST record from the Ontong-Java plateau[12]. The amplitude of a full glacial SST cycle in the WPWP is on average 2.2 ± 0.7 °C during the late Pleistocene (6–850 kyr ago), and 1.5 ± 0.6 °C during the early Pleistocene (850–1,750 kyr ago). As glacial SSTs are relatively constant at 25.9 ± 0.2 °C throughout the Pleistocene, the changes in glacial–interglacial amplitude reflect mainly variability in interglacial maxima. Throughout the record, the increase in SST during glacial terminations leads the deglacial change in $\delta^{18}O_{G.\ ruber}$. Cross-spectral analysis shows that between 0 and 0.85 Myr ago the SST lead is about 4 ± 4 kyr in the eccentricity band, in agreement with results from other late-Pleistocene equatorial Pacific records[4,12,14]. Between 0.85 and 1.75 Myr ago the SST lead is about 10 ± 4 kyr in the dominant 41-kyr band (Fig. 2). The early-Pleistocene average SST is 27.1 ± 1 °C, which is not statistically different from the late-Pleistocene average SST of 27.2 ± 1 °C; and indicates that long-term temperature in the WPWP is not influenced by the Mid-Pleistocene Revolution.

Our record of surface water $\delta^{18}O_{water}$ (used as a proxy of surface salinity; Fig. 1), calculated from Mg/Ca and $\delta^{18}O_{G.ruber}$ data, provides a useful assessment of hydrological variations in the WPWP across the mid-Pleistocene transition. The record indicates the long-term stability of $\delta^{18}O_{water}$ (average 0.66 ± 0.25‰ and 0.65 ± 0.25‰ for early and late Pleistocene, respectively). This contrasts with the record of deep-water benthic foraminiferal $\delta^{18}O$ (see, for example, Fig. 3), which shows a long-term trend of

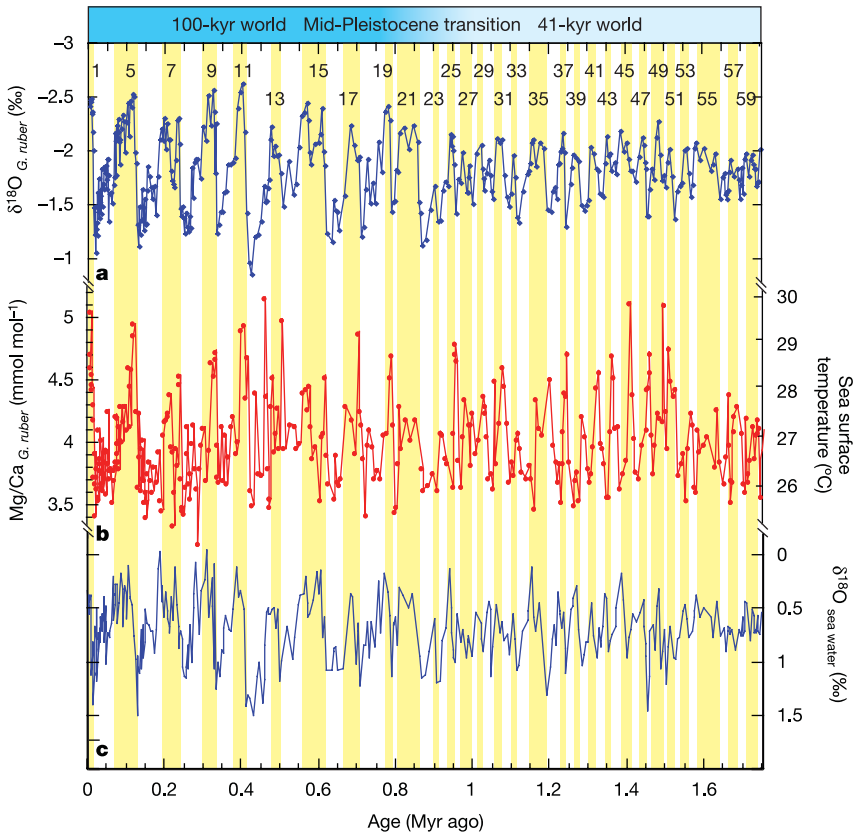

Figure 1 Pleistocene reconstruction of surface water changes in the WPWP from the IMAGES core MD97-2140. **a**, **b**, Planktonic foraminiferal records (*G. ruber*) of $\delta^{18}O$ (**a**) and Mg/Ca SST (**b**) from IMAGES core MD97-2140 (Eauripik rise 2° 02′ N, 141° 46′ E, 2,547 m). SST estimates were calculated using the core-top calibration[29] of Mg/Ca = 0.30 × exp(0.095 × SST). **c**, $\delta^{18}O_{sea\ water}$ computed using the isotopic equation of ref. 30. Interglacial periods are numbered following the terminology of SPECMAP (ref. 13 and references therein). Note the concomitant increase in interglacial $\delta^{18}O_{G.\ ruber}$ with decreasing SSTs between 1.2 and 0.85 Myr ago, before the onset of the late Pleistocene 100-kyr glaciations.

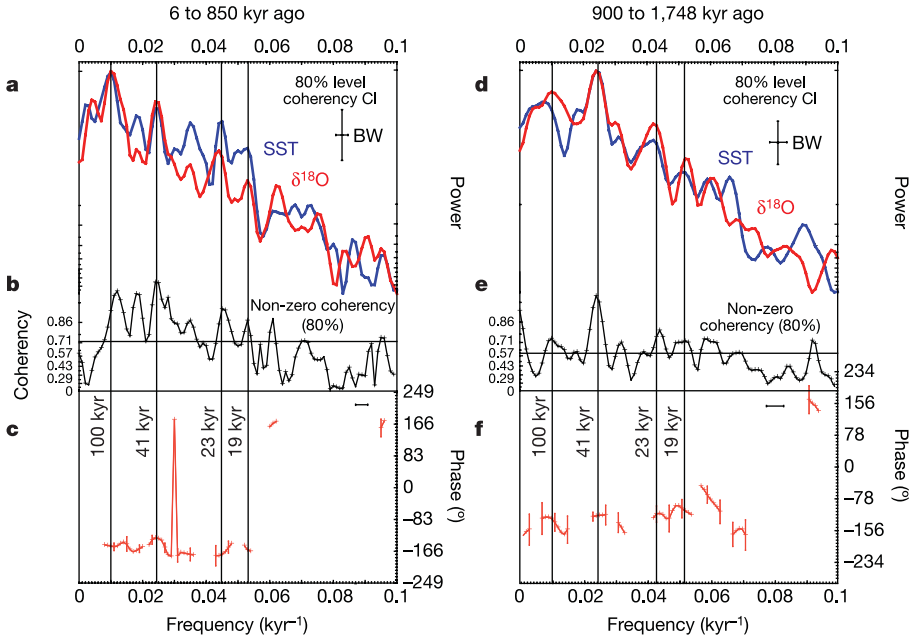

Figure 2 Comparison of spectral analysis of $\delta^{18}O$ and Mg/Ca-derived SST records from MD97-2140 in the late and early Pleistocene. **a**, Time interval from 6 to 850 kyr ago; **b**, time interval from 900 to 1,748 kyr ago. Panels also present the coherency (**b**, **e**) and phase relationship (**c**, **f**) obtained from cross-spectral analysis between the MD97-2140 $\delta^{18}O$ and SST for each period. The confidence interval (CI) at the 80% significance level and the bandwidth (BW) used for the spectral analysis are displayed.

increasing $\delta^{18}O$ through the Pleistocene, presumably reflecting expansion of continental ice. We suggest that the effect of Pleistocene ice-sheet growths on surface WPWP $\delta^{18}O$ was compensated by progressive regional freshening. Nowadays, although advection of surface water might also have affected the hydrography of the WPWP, the surface salinity is mainly influenced by the local precipitation–evaporation balance[15]. Our data suggest that although the thermal response of the WPWP to the mid-Pleistocene transition changes was small, there was a substantial effect on the regional hydrological cycle.

Recently, it has been suggested that the increase in the Pacific zonal SST contrast and development of strong Walker circulation—driven by enhanced upwelling and cooling of surface waters in the eastern equatorial Pacific (ODP site 851, 2° 46′ N, 110° 34′ W)—might have had a strong influence on the climate response to radiative changes, thus contributing to the Pliocene cooling trend[16]. A further cooling of the eastern equatorial Pacific cold tongue, also attributed to changes in upwelling, occurred during the mid-Pleistocene (between 1.2 and 0.8 Myr ago), as inferred from an alkenone-based SST record of ODP site 846 (3° 6′ S, 90° 49′ W)[4]. Our new record (MD97-2140) suggests, however, that this cooling was restricted to the upwelling region and did not affect the greater tropical band. This conclusion is supported by evidence from the Atlantic Ocean, where a subtropical record from the Benguela upwelling region shows significant cooling during the mid-Pleistocene transition[3] (Fig. 3), whereas another subtropical record of ODP site 1077 (10° 26′ E, 5° 10′ S) does not show any long-term SST change across the mid-Pleistocene transition[17]. Combined, these observations suggest that the mid-Pleistocene cooling was restricted to upwelling regions, whereas surface temperatures remained at the same mean level before and after 0.8 Myr ago in the WPWP and probably in most of the tropical oceans.

In the modern ocean, the interannual variability in the temperature difference (ΔSST) between the sites of MD97-2140 and ODP846 is highly correlated with the Southern Oscillation index ($r^2 \approx 0.6$), an index of the ENSO; a larger ΔSST, primarily a result of enhanced upwelling in the eastern equatorial Pacific, occurs during the cold phase of ENSO (La Niña) and a smaller ΔSST during the warm phase (El Niño). La Niña events, which are periods of intensified low-latitude zonal winds, and enhanced precipitation in the western equatorial Pacific are also characterized by fresher sea surface waters at the site of the MD97-2140 (ref. 18). Although a direct comparison of the alkenone-derived SST record from ODP846 and the Mg/Ca SST record of MD97-2140 might be problematic owing to possible discrepancies between the two proxies[19], recent multi-proxy studies indicate that their respective estimates generally agree to within 1 °C in the equatorial Pacific[20]. Taken at face value, the comparison indicates a long-term change in the ΔSST between the cold tongue and the warm pool from the early to late Pleistocene (Fig. 3). The most notable feature of the ΔSST reconstruction is an increase from ~3.5 to ~5 °C that occurred during the interval between 1.2 and 0.8 Myr ago, coincident with the mid-Pleistocene increase in ice volume as reflected in the positive shift in the benthic foraminiferal $\delta^{18}O$ record of ODP846 (Fig. 3). The increase in ΔSST gradient between the eastern and western equatorial Pacific sites and inferred freshening at MD97-2140 are consistent with a change in the mean climate state from an El Niño-like state to more La Niña-like conditions, which implies an intensification of the Walker circulation during the mid-Pleistocene (Fig. 3).

Most mechanisms proposed to explain the mid-Pleistocene shift from 41-kyr to 100-kyr periodicity in climate records invoke a gradual global cooling during the Pleistocene, until a threshold is passed around 0.85 Myr ago, when feedbacks exerted by continental and/or marine ice-sheet dynamics are assumed to have become preponderant[1,21,22]. This gradual global cooling scenario is attributed by some to a decrease in atmospheric p_{CO_2}, and its effect on radiative forcing, during the early Pleistocene[1]. Evidence for this 'cooling' hypothesis comes primarily from alkenone-based SST reconstructions from the upwelling regions, but is not supported by our WPWP record. Moreover, as the long-term control of equatorial Pacific SSTs results from the combined effects of greenhouse gases (mainly water vapour, CO_2 and CH_4) and albedo[5,6], our new SST record provides a different perspective on Pleistocene climate evolution. The long-term stability of WPWP temperatures during the Pleistocene implies little change in the tropical net

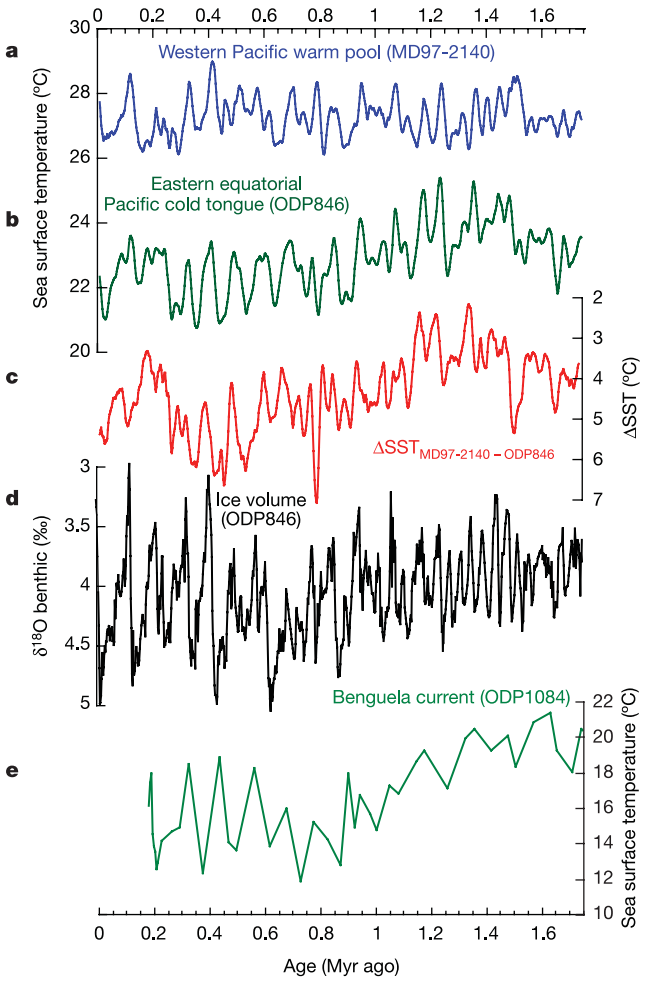

Figure 3 Comparison of the WPWP Pleistocene climatic evolution with palaeoclimatic records from different regions. **a**, **b**, Mg/Ca-derived SST record from MD97-2140 (**a**) in the WPWP and the alkenone-derived SST record of ODP846 (**b**) from the cold tongue in the eastern equatorial Pacific[4]. Both records are smoothed with a 20-kyr moving average; **c**, shows the $\Delta SST_{MD97\text{-}2140-ODP846}$ record as a proxy of the zonal surface thermal gradient between the western and the eastern equatorial Pacific. Note the reversed temperature scale. **d**, The eastern equatorial Pacific $\delta^{18}O$ benthic (site ODP 846) is used as a proxy of ice volume[28]. **e**, Smoothed with a 20-kyr moving average, the Benguela upwelling alkenone-based SST record[3].

radiative budget. This relative stability challenges the decreasing atmospheric p_{CO_2} scenario assumed for the onset of the mid-Pleistocene large 100-kyr glaciations[1].

An alternative view is that nonlinear coupled ocean–atmosphere dynamics that regulate the equatorial Pacific climate, might have played a more significant role than changes in radiative forcing in the mid-Pleistocene transition; in agreement with recent studies of the Pliocene initiation of Northern Hemisphere glaciation[16]. The increased temperature contrast between the eastern equatorial Pacific upwelling regions and the thermally stable WPWP in the mid-Pleistocene probably led to the intensification of the Walker circulation. This strengthening of the zonal Pacific atmospheric circulation is further supported by the surface freshening of the WPWP. Both observations imply drastic changes in the equatorial Pacific SST and salinity patterns across the mid-Pleistocene transition. These changes might have led to atmospheric processes[11] and oceanic interactions[23], which could have altered the meridional heat and moisture transfer to the Northern Hemisphere ice sheets during the mid-Pleistocene transition and thus contributed to the Northern Hemisphere glaciation. □

Methods

Analytical methods

Isotope measurements were done at LSCE (Gif-sur-Yvette, France), using a Kiel device coupled to a Finnigan MAT 251 mass spectrometer. The external precision of $\delta^{18}O$ analysis was 0.05‰, as determined by repeated measurements of a standard carbonate material, NBS19. Mg/Ca measurements were done at Rutgers University using Finnigan Element 1 inductively coupled plasma mass spectrometry (ICP-MS), following the analytical protocol detailed in ref. 24. Samples were prepared using the Boyle and Keigwin method[25], excluding the reductive step. The long-term external precision of Mg/Ca analysis was about 4.5% (1 σ, relative standard deviation, r.s.d.) as determined by repeated measurements of three consistency standards with Mg/Ca ratios varying from 1.2 to 7 mmol mol^{-1}. This is equivalent to ±0.5 °C analytical error in the core record. The planktonic foraminifer *G. ruber* was chosen for this study because this species lives strictly in the mixed layer, and therefore its geochemical composition reflects the overlying surface hydrography. Moreover, fluxes of *G. ruber* to the sediment in the WPWP do not show any evidence of a seasonal bias, circumventing the possibility of a seasonal effect on the estimated SST[26].

Age model and time-series analyses

The MD97-2140 $\delta^{18}O_{G.\ ruber}$ record was tuned to the astronomically calibrated ODP677 $\delta^{18}O_{G.\ ruber}$ record[13] located in the eastern equatorial Pacific (Fig. 1), yielding chronology consistent with major micro-paleontological (disappearance of *G. ruber* pink variety) and palaeomagnetic (Brunhes–Matuyama boundary[27]) events. The average sedimentation rate is ~2 cm kyr^{-1} throughout the last 1,755 kyr recovered by the core. The core was sampled every 10 cm for both isotopic and trace-metal analyses, yielding ~5-kyr resolution. To calculate the equatorial zonal temperature gradient, we first matched the MD97-2140 $\delta^{18}O_{G.\ ruber}$ record to the ODP846 $\delta^{18}O_{benthic}$ record[28] to get a consistent timescale for both records. The zonal thermal gradient was calculated as the difference: $\Delta SST = SST_{MD97\text{-}2140} - SST_{ODP846}$. To compute the amplitude of glacial–interglacial changes in SST and $\delta^{18}O$, we first defined the MIS using the $\delta^{18}O_{G.\ ruber}$ correlation to the ODP846 benthic reference curve[28]. Then we averaged the downcore values within each MIS. The amplitude of glacial–interglacial variations was finally computed by subtracting the interglacial estimates from the glacial ones. Spectral analyses were performed using the Arand software package of Brown University (available at http://www.ngdc.noaa.gov/paleo/softlib/), after linear detrending of time series. All MD97-2140 data are archived on the NGDC-NOAA palaeoclimate database website: http://www.ngdc.noaa.gov/paleo/paleo.html.

Received 12 July; accepted 15 November 2004; doi:10.1038/nature03189.

1. Berger, A., Li, X. S. & Loutre, M.-F. Modelling northern hemisphere ice volume over the last 3 Ma. *Quat. Sci. Rev.* **18,** 1–11 (1999).
2. Raymo, M. E. The timing of major climate terminations. *Paleoceanography* **12,** 577–585 (1997).
3. Marlow, J. R., Lange, C. B., Wefer, G. & Rosell-Mele, A. Upwelling intensification as part of the Pliocene-Pleistocene climate transition. *Science* **290,** 2288–2291 (2000).
4. Liu, Z. & Herbert, T. D. High-latitude influence on the eastern equatorial Pacific climate in the early Pleistocene epoch. *Nature* **427,** 720–723 (2004).
5. Lea, D. W. The 100,000 year cycle in tropical SST, greenhouse forcing, and climate sensitivity. *J. Clim.* **17,** 2170–2179 (2004).
6. Broccoli, A. J. Tropical cooling at the last glacial maximum: an atmosphere-mixed layer ocean model simulation. *J. Clim.* **13,** 951–976 (2000).
7. Conkright, M. *et al. World Ocean Atlas 1998* [CD-ROM] (Data Set Documentation 16, NODC, Silver Springs, Maryland, 1998).
8. Ropelewski, C. F. & Halpert, M. S. Global and regional scale precipitation patterns associated with the El Niño/Southern Oscillation. *Mon. Weath. Rev.* **115,** 1606–1626 (1986).
9. Halpert, M. S. & Ropelewski, C. F. Surface temperature patterns associated with the Southern Oscillation. *J. Clim.* **5,** 577–593 (1992).
10. Sun, D. Z. Possible effect of an increase in the warm-pool SST on the magnitude of El Nino warming. *J. Clim.* **16,** 185–205 (2003).
11. Yin, J. H. & Battisti, D. S. The importance of tropical sea surface temperature patterns in simulations of Last Glacial Maximum climate. *J. Clim.* **14,** 565–581 (2001).
12. Lea, D. W., Pak, D. K. & Spero, H. J. Climate impact of late quaternary equatorial Pacific sea surface temperature variations. *Science* **289,** 1719–1724 (2000).
13. Shackleton, N. J., Berger, A. & Peltier, W. R. An alternative astronomical calibration of the lower Pleistocene timescale based on ODP Site 677. *Trans. R. Soc. Edinb. Earth Sci.* **81,** 251–261 (1990).
14. Visser, K., Thunell, R. C. & Stott, L. Magnitude and timing of temperature change in the Indo-Pacific warm pool during deglaciation. *Nature* **421,** 152–155 (2003).
15. Delcroix, T. Observed surface oceanic and atmospheric variability in the tropical Pacific at seasonal and ENSO timescales: a tentative overview. *J. Geophys. Res.* **103,** 18611–18633 (1998).
16. Ravelo, A. C., Andreasen, D. H., Lyle, M., Lyle, A. O. & Wara, M. W. Regional climate shifts caused by gradual global cooling in the Pliocene epoch. *Nature* **429,** 263–267 (2004).
17. Schefuß, E., Schouton, S., Fred Jansen, J. H. & Sinninghe Damste, J. S. African vegetation controlled by tropical sea surface temperatures in the mid-Pleistocene period. *Nature* **422,** 418–421 (2003).
18. Delcroix, T. & McPhaden, M. Interannual sea surface salinity and temperature changes in the western Pacific warm pool during 1992–2000. *J. Geophys. Res. Oceans* **107,** 22135–22150 (2002).
19. Nürnberg, D., Mueller, A. & Schneider, R. R. Paleo-sea surface temperature calculations in the equatorial east Atlantic from Mg/Ca ratios in planktic foraminifers: A comparison to sea surface temperature estimates from Uk'37, oxygen isotopes, and foraminiferal transfer function. *Paleoceanography* **15,** 124–134 (2000).
20. Kiefer, T. & Kienast, M. Patterns of deglacial warming in the Pacific Ocean: a review with emphasis on the time interval of Heinrich event 1. *Quat. Sci. Rev.* (in the press).
21. Imbrie, J. *et al.* On the structure and origin of major glaciation cycles. 2. The 100,000-year cycle. *Paleoceanography* **8,** 699–735 (1993).
22. Tziperman, E. & Gildor, H. On the mid-Pleistocene transition to 100- kyrr glacial cycles and the

asymmetry between glaciation and deglaciation times. *Paleoceanography* **18,** doi:10.1029/2001PA000627 (2003).
23. Philander, S. G. & Fedorov, A. V. Role of tropics in changing the response to Milankovitch forcing some three million years ago. *Paleoceanography* **18,** doi:10.129/2002PA000837 (2003).
24. Rosenthal, Y., Field, F. & Sherrell, R. M. Precise determination of element/calcium ratios in calcareous samples using sector field inductively coupled plasma mass spectrometry. *Anal. Chem.* **71,** 3248–3253 (1999).
25. Boyle, E. A. & Keigwin, L. D. Comparison of Atlantic and Pacific paleochemical records for the last 250,000 years: changes in deep ocean circulation and chemical inventories. *Earth Planet. Sci. Lett.* **76,** 135–150 (1985).
26. Kawahata, H., Nishimura, A. & Gagan, M. K. Seasonal change in foraminiferal production in the western equatorial Pacific warm pool: evidence from sediment trap experiments. *Deep-sea Res. II* **49,** 2783–2800 (2002).
27. Carcaillet, J. T., Thouveny, N. & Bourles, D. L. Geomagnetic moment instability between 0.6 and 1.3 Ma from cosmonuclide evidence. *Geophys. Res. Lett.* **30,** doi:10.1029/2003GL017550 (2003).
28. Mix, A. C. *et al.* Benthic foraminiferal stable isotope stratigraphy of Site 846; 0–1.8 Ma. *Proc. ODP Sci. Res.* **138,** 839–854 (1995).
29. Rosenthal, Y. & Lohmann, G. P. Accurate estimation of sea surface temperatures using dissolution-corrected calibrations for Mg/Ca paleothermometry. *Paleoceanography* **17,** doi: 1029/2001PA000749 (2002).
30. Bemis, B. E., Spero, H. J., Bijma, J. & Lea, D. W. Reevaluation of the oxygen isotopic composition of planktonic foraminifera: experimental results and revised paleotemperature equations. *Paleoceanography* **13,** 150–160 (1998).

Supplementary Information accompanies the paper on **www.nature.com/nature**.

Acknowledgements The support of French MENRT, TAAF, CNRS/INSU and IPEV to the Marion-Dufresne and the IMAGES Program was necessary to perform this work. We are grateful to N. Buchet, B. Le Coat, P. Field and S. Perron-Cushman for technical help, and to A. Broccoli, A. C. Ravelo, D. Andreasen and C. Lévi for comments. This study was partially supported by Rutgers' post-doctoral fellowship to T.d.G.-T. and by the National Science Foundation to Y.R.

Competing interests statement The authors declare that they have no competing financial interests.

Correspondence and requests for materials should be addressed to T.d.G.-T. (garidel@marine.rutgers.edu).

Long-term sensitivity of soil carbon turnover to warming

W. Knorr[1], I. C. Prentice[1,2], J. I. House[1,2] & E. A. Holland[1,3]

[1]*Max Planck Institute for Biogeochemistry, PO Box 100164, D-07701 Jena, Germany*
[2]*QUEST, Department of Earth Sciences, University of Bristol, Wills Memorial Building, Bristol BS8 1RJ, UK*
[3]*National Center for Atmospheric Research, PO Box 3000, Boulder, Colorado 80305, USA*

The sensitivity of soil carbon to warming is a major uncertainty in projections of carbon dioxide concentration and climate[1]. Experimental studies overwhelmingly indicate increased soil organic carbon (SOC) decomposition[2–8] at higher temperatures, resulting in increased carbon dioxide emissions from soils. However, recent findings have been cited as evidence against increased soil carbon emissions in a warmer world[9,10]. In soil warming experiments, the initially increased carbon dioxide efflux returns to pre-warming rates within one to three years[10–14], and apparent carbon pool turnover times are insensitive to temperature[15]. It has already been suggested that the apparent lack of temperature dependence could be an artefact due to neglecting the extreme heterogeneity of soil carbon[16], but no explicit model has yet been presented that can reconcile all the above findings. Here we present a simple three-pool model that partitions SOC into components with different intrinsic turnover rates. Using this model, we show that the results of all the soil-warming experiments are compatible with long-term temperature sensitivity of SOC turnover: they can be explained by rapid depletion of labile SOC combined with the negligible response of non-labile SOC on experimental timescales. Furthermore, we present evidence that non-labile SOC is more sensitive to temperature than labile SOC, implying that the long-term positive feedback of soil decomposition in a warming world may be even stronger than predicted by global models[1,17–20].

The short-term temperature dependence of decomposition and heterotrophic respiration in soils is well established experimentally (see, for example, refs 2–8), and is modelled either by a constant Q_{10} value of ~2 (Q_{10} is the proportional increase in reaction rate for a 10 K warming) or more accurately by the Arrhenius equation or slight modifications thereof[3,5]. This short-term response conceals enormous heterogeneity in SOC: soils include compounds with intrinsic turnover times (that is, turnover times at a reference temperature) ranging from <1 yr to $>6\times10^3$ yr (refs 4, 16, 21). Geographical patterns generally show younger SOC ^{14}C ages in warmer climates[4,16,21,22], consistent with the hypothesis that climatic warming should reduce global SOC by reducing residence times.

It is well established that a one-pool representation of SOC dynamics is insufficient to explain experimental findings from warming and incubation experiments[5,16]. But no model has yet been presented that is able to reconcile the above observations with refs 10–15. To this end, we used experimental data from ref. 6 to fit simple illustrative models of SOC decomposition. The data were derived from temperature-controlled incubations of an undisturbed soil from a tropical rain forest site with a mean annual temperature of 27 °C. Carbon dioxide (CO_2) efflux was measured at ten intervals through a 24-week period (see Methods). The soil was taken to consist of n pools of carbon content c_i, each decaying at a temperature-dependent rate k_i over time t:

$$\mathrm{d}c_i(t)/\mathrm{d}t = -k_i c_i(t) \quad (1)$$

We considered Arrhenius models with a single reference decay rate A for all pools, and n activation energy values E_i:

$$k_i(T_k) = A\exp(-E_i/RT_k) \quad (2)$$

where T_k is soil temperature in kelvin and A the theoretical decay rate at $E_i = 0$; R is the universal gas constant.

We started by fitting a model with $n = 1$, then increased n until no significant improvement of a χ^2 criterion was obtained (see Methods). This procedure selected a model with $n = 2$ (Table 1a). The time-course of CO_2 efflux during the 24-week observation period is thus appropriately modelled by the decay of two SOC pools following Arrhenius kinetics but differing in activation energy. But the total soil carbon content implied by the two-pool decay models (Table 1) is far less than the measured initial carbon content of 29.4 g C per kg soil. We therefore added a third pool, effectively inert over the timescale of the experiment, which accounts for ~95% of SOC. The fitted turnover time for this pool is arbitrarily large. A lower limit for its activation energy (see Methods) is 68,000 J mol^{-1}, implying a turnover time of 260 yr at 25 °C.

Adopting the three-pool Arrhenius model with $E_3 = 68{,}000$ Jmol^{-1}, we first reconsider the analysis of incubation experiments in ref. 15. A one-pool model based on equation (1) was used there to analyse the fractional decay of SOC after incubation for 1 yr. Inverting the solution to equation (1) for a single SOC pool gives an apparent turnover time, τ:

$$\tau = -t_1/\ln[c(t_1)/c(0)] \quad (3)$$

where t_1 is the time at the end of the incubation[15]. Applying this definition to modelled total soil carbon content $c(t_1)$, with $t_1 = 1$ yr, markedly reduces the apparent sensitivity of turnover time to temperature despite the built-in temperature dependence of all the rate constants (Fig. 1a). This paradox arises because total soil carbon $c(t)$ is dominated by the slowest pool; over a year, the two faster pools have largely decayed. The apparent turnover time is then closely approximated by $c_3(0)/c(0)$. This ratio contains no